# Long-Horizon Robust Direct Model Predictive Control for Medium-Voltage Induction Motor Drives with Reduced Computational Complexity

Andrei Tregubov, *Student Member, IEEE*, Petros Karamanakos, *Senior Member, IEEE*,
and Ludovico Ortombina, *Member, IEEE*

*Abstract*—This paper proposes a long-horizon direct model predictive control (MPC) with reference tracking for medium-voltage (MV) drives that achieves favorable steady-state and transient behavior. However, as MPC is a model-based method, it is susceptible to parameter mismatches and variations of the machine. Moreover, even though a long prediction horizon significantly improves the steady-state behavior of the drive, it significantly increases the computational complexity of the direct MPC problem, rendering its real-time implementation a challenging—if not impossible—task. Motivated by these shortcomings of long-horizon direct MPC, this paper also aims to address them by enhancing the robustness of the developed control strategy, while keeping its computational complexity modest. To achieve the former, a prediction model suitable for MV drive systems is adopted that facilitates the effective estimation of the total leakage inductance of the machine. For the latter, the objective function of the MPC problem is formulated such that, even though the drive behavior is computed over a long prediction interval, only a few changes in the candidate switch positions are considered. The effectiveness of the proposed modeling, control, and estimation approaches is validated with hardware-in-the-loop (HIL) tests for an MV drive consisting of a three-level neutral point clamped (NPC) inverter and an induction machine (IM).

*Index Terms*—AC drives, medium-voltage (MV) drives, model predictive control (MPC), direct control, robust control, hardware-in-the-loop (HIL) simulations.

## I. INTRODUCTION

Over the last years, the advanced processing capabilities of modern microprocessors have facilitated the development of high-performance rapid control prototyping platforms for power electronics [2]. Such a technological advancement, combined with a growing demand for high-efficiency variable speed drive (VSD) systems—including medium-voltage (MV) VSDs—have stimulated the increasing interest of the power electronics community in model predictive control (MPC). This is reflected, e.g., in the exponential growth of publications in the said research area since the early 2000s [3]. Even though several derivatives of MPC have been introduced over the years, the most widely adopted strategy—at least in academia—is direct MPC with reference tracking, also referred to as finite control set MPC (FCS-MPC) [3].

A. Tregubov and P. Karamanakos are with the Faculty of Information Technology and Communication Sciences, Tampere University, 33101 Tampere, Finland; e-mail: andrei.tregubov@tuni.fi, p.karamanakos@ieee.org

L. Ortombina is with the Department of Industrial Engineering, University of Padova, 35122 Padova, Italy; e-mail: ludovico.ortombina@unipd.it

Despite the fact that FCS-MPC appears as an attractive alternative to established control methods [4], it has intrinsic drawbacks. One of them stems from the fact that the computational burden of the optimization problem underlying FCS-MPC increases exponentially with the length of the prediction horizon and the number of the output voltage levels of the power converter. As a result, one-step horizon is typically used, but, alas, at the expense of improved performance and guaranteed stability that long horizons can offer [3], [5].

To address this issue, and thus facilitate the real-time implementation of long-horizon FCS-MPC, some methods have been proposed that aim to reduce the computational complexity of the associated optimization problem, such as dedicated branch-and-bound techniques [6], or prediction horizons of nontrivial form [7]. In this direction, and as far as long-horizon FCS-MPC for three-level power converters is concerned, the branch-and-bound strategy called sphere decoder was implemented in real time in [8]–[10]. It is worth noting that the control platform used in [8] was a dSPACE, whereas works [9] and [10] implemented the long-horizon FCS-MPC algorithm on a field-programmable gate array (FPGA). Nevertheless, regardless of the control platform, the sphere decoder is executed in a sequential manner, implying that the ability of an FPGA to perform intensive calculations in a highly pipelined and/or parallelized manner was not exploited [11]. On the other hand, [12] implemented FCS-MPC with a nontrivial horizon on an FPGA by effectively pipelining the optimization procedure. However, as a "certificate of optimality" is not provided at the end of the optimization process, optimality is not ensured at all operating points. Hence, it can be concluded that the design of long horizon FCS-MPC remains a nontrivial and challenging task.

Another drawback of FCS-MPC is that its performance is dependent on the accuracy of the prediction model. The latter, even though typically accurate when power electronic applications are of interest, is subject to model variations and mismatches that can adversely affect the system performance, especially when long horizons are employed [11]. For example, when induction motor (IM) drives are of interest, the values of the machine inductances and resistances may change in time due to, e.g., changes in the temperature or saturation of the magnetic material. Such modeling mismatches may lead to prediction errors that accumulate as the horizon length

increases, thus resulting in suboptimal control actions. Hence, FCS-MPC needs to be equipped with tools that can enhance its robustness to such uncertainties and variations. To this end, FCS-MPC for IM drives can be augmented with an element of integrating nature [13], or an external disturbance observer [14]–[16]. Such methods, however, can increase the complexity of the closed-loop controller design, or even the computational complexity as they can be computationally intensive.

An alternative is to employ system identification algorithms. Such methods are either white-box model-based approaches, since they assume full knowledge of the system [17]–[20], or they do not depend on the model at all, i.e., they are black-box methods [21], [22]. The former techniques, however, cannot simultaneously estimate all the system parameters, meaning that combinations of different sources of uncertainties/model mismatches are usually not considered. As a result, the performance of such methods is not the most desired for a wide range of operating conditions. For example, the fidelity of the model reference adaptive system (MRAS) approach adopted in [20] to estimate the mutual inductance degrades linearly with the increasing IM load torque. Moreover, as the MRAS adaptive model depends, among others, on the rotor resistance, a reactive power MRAS (Q-MRAS) scheme is implemented in parallel to improve the estimation accuracy of the machine parameters. This, however, adds a significant computational overhead.

As for the black-box methods, which have been mostly implemented for two-level inverters, their accuracy relies on measurements of the input (e.g., applied voltage) and output (e.g., load current), and intrinsic look-up tables [23]. Moreover, the acquired data are processed by computationally demanding identification techniques, such as data fitting methods, which further increase the computational requirements of MPC. Hence, as can be understood, it is desired that the aforementioned auxiliary tools should come with low computational complexity not to further tax the already high computational load of long-horizon FCS-MPC.

Motivated by the above, this paper proposes a long-horizon FCS-MPC for MV IM VSD systems that achieves favorable steady-state and transient behavior while addressing the two main drawbacks of FCS-MPC. More specifically, the proposed algorithm (a) has modest computational complexity, and (b) shows a high degree of robustness.[1] To achieve the former, the MPC problem is formulated by taking advantage of the fact that MV drives need to operate at low switching frequencies of a few hundred hertz, meaning that the control action changes only a few times within the fundamental period. In doing so, two different horizons are defined in the MPC problem, namely the control and prediction horizons, that can be manipulated to keep the computational complexity at bay while still achieving a superior drive performance.

[1]This paper is an extension of [1]. Herein, as compared with [1], a deeper theoretical analysis of the proposed method is presented along with its verification with real-time tests performed in a hardware-in-the-loop (HIL) environment.
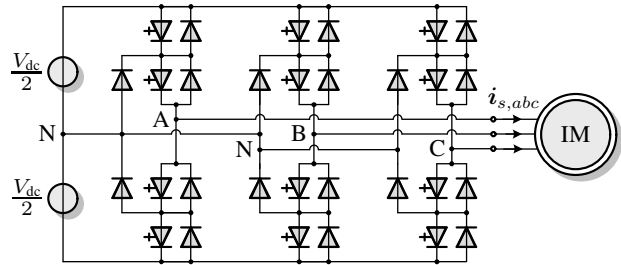


Fig. 1: Three-level NPC voltage-source inverter (VSI) driving an IM.

TABLE I: MV VSD rated values and parameters.

| Parameter | Value |
|---|---|
| Rated voltage $V_R$ | 3300 V |
| Rated current $I_R$ | 356 A |
| Real power $P_R$ | 1.646 MW |
| Apparent power $S_R$ | 2.035 MVA |
| Angular stator frequency $\omega_{sR}$ | $2\pi 50$ rad/s |
| Rotational speed $\omega_{mR}$ | 596 rpm |
| Stator resistance $R_s$ | 57.61 mΩ |
| Rotor resistance $R_r$ | 48.89 mΩ |
| Stator leakage inductance $L_{ls}$ | 2.544 mH |
| Rotor leakage inductance $L_{lr}$ | 1.881 mH |
| Main inductance $L_m$ | 40.01 mH |
| Dc-link voltage $V_{dc}$ | 5.2 kV |

The latter is accomplished by deriving a prediction model of the drive system that allows for the adoption of a simple, yet effective, estimation algorithm. The presented real-time hardware-in-the-loop (HIL) simulations based on an MV VSD system demonstrate the performance benefits of the proposed approach.

The remainder of this paper is organized as follows. Section II presents the adopted model of the MV VSD system. Following, the proposed FCS-MPC algorithm is presented in Section III along with the controller design choices. Section IV provides the robustness analysis of the developed control strategy and identifies which system parameter variations mostly affect its performance. Subsequently, the design of the proposed estimation technique is provided in Section V, while its performance based on real-time HIL simulations is presented in Section VI. Finally, conclusions are drawn in Section VII.

## II. MODELING

Consider the MV VSD system in Fig. 1 consisting of three-level neutral point clamped (NPC) inverter and an IM with the rated values and parameters provided in Table I. The aim is to develop an FCS-MPC algorithm to control the drive system. Since such a control method requires an accurate model of the plant, the differential equations that fully describe the system dynamics are derived in this section. To do so, the per unit (p.u.) system and the $\alpha\beta$-reference frame are adopted in this work. Moreover, for simplicity, the neutral point potential $v_n$ is assumed to be zero and the dc-link voltage constant and equal to $V_{dc}$.

Based on the above, the inverter output voltage $\boldsymbol{v}_{\text{inv}}$ (which is equal to the stator voltage $\boldsymbol{v}_s$) is[2]

$$\boldsymbol{v}_{\text{inv}} = \boldsymbol{v}_s = \frac{V_{\text{dc}}}{2} \boldsymbol{K} \begin{bmatrix} u_a & u_b & u_c \end{bmatrix}^T, \qquad (1)$$

where $\boldsymbol{K}$ is the reduced Clarke transformation matrix

$$\boldsymbol{K} = \frac{2}{3} \begin{bmatrix} 1 & -\frac{1}{2} & -\frac{1}{2} \\ 0 & \frac{\sqrt{3}}{2} & -\frac{\sqrt{3}}{2} \end{bmatrix}, \qquad (2)$$

and $\boldsymbol{u}_{abc} = \begin{bmatrix} u_a & u_b & u_c \end{bmatrix}^T$ is the three-phase switch position, with $u_x \in \mathcal{U} = \{-1, 0, 1\}$, $x \in \{a, b, c\}$, being the single-phase switch position.

Most of the FCS-MPC methods typically employ the T-equivalent model of an IM, see Fig. 2(a), where $R_s$ and $R_r$ stand for the stator and rotor resistances, respectively, while $X_{ls}$, $X_{lr}$, and $X_m$ are the stator leakage, rotor leakage, and mutual reactances, respectively [24]. However, this model is overparametrized, while observability and identifiability of the machine parameters are not achieved [25]. These issues, nonetheless, can be tackled when using the so-called inverse-Γ model, shown in Fig. 2(b). Note that the two representations of the IM are equivalent and no loss of information or accuracy is entailed [26].

The derivation of the inverse-Γ model is based on providing the same input impedance as the T-model. Hence, the stator voltage $\boldsymbol{v}_s$, current $\boldsymbol{i}_s$, and flux $\boldsymbol{\psi}_s$ are the same in both IM representations. Moreover, the rotor current and flux are defined with the help of the transformation coefficient $\gamma = X_m/X_r$ as $\bar{\boldsymbol{i}}_r = \boldsymbol{i}_r/\gamma$ and $\bar{\boldsymbol{\psi}}_r = \gamma \boldsymbol{\psi}_r$, where the overline denotes variables in the inverse-Γ model, and $X_r = X_{lr} + X_m$ is the rotor self-reactance. Based on the above definitions, the equivalent circuit representation in Fig. 2(b) is obtained with the following parameters

$$\bar{X}_m = \gamma X_m, \qquad (3a)$$
$$\bar{R}_r = \gamma^2 R_r, \qquad (3b)$$
$$X_\sigma = X_s - X_m^2/X_r, \qquad (3c)$$

where $X_\sigma$ is the total leakage reactance, and $X_s = X_{ls} + X_m$ is the stator self-reactance.

A closer comparison between Figs. 2(a) and 2(b) shows the advantage of adopting the inverse-Γ IM model. Specifically, as can be deduced from (3c), the impact of the rotor $X_{lr}$ and stator $X_{ls}$ leakage reactances in the T-equivalent model is mostly captured by the total leakage reactance $X_\sigma$ in the inverse-Γ model. This will be utilized when designing the estimation algorithm, see Section V.

Given the equivalent circuit in Fig. 2(b), the state-space model of the MV drive system can be derived. Specifically, by defining the three-phase switch position $\boldsymbol{u}_{abc} \in \mathcal{U} = \mathcal{U}^3$ as the input of the system, the stator current and flux as state variables, i.e., $\boldsymbol{x} = [\boldsymbol{i}_s^T \ \boldsymbol{\psi}_s^T]^T \in \mathbb{R}^4$, and the stator current as the system output, i.e., $\boldsymbol{y} = \boldsymbol{i}_s \in \mathbb{R}^2$, the continuous-time

[2]To simplify the notation, the subscript for variables in the $\alpha\beta$-plane is omitted. Variables in the $abc$-plane are indicated by the corresponding subscript.
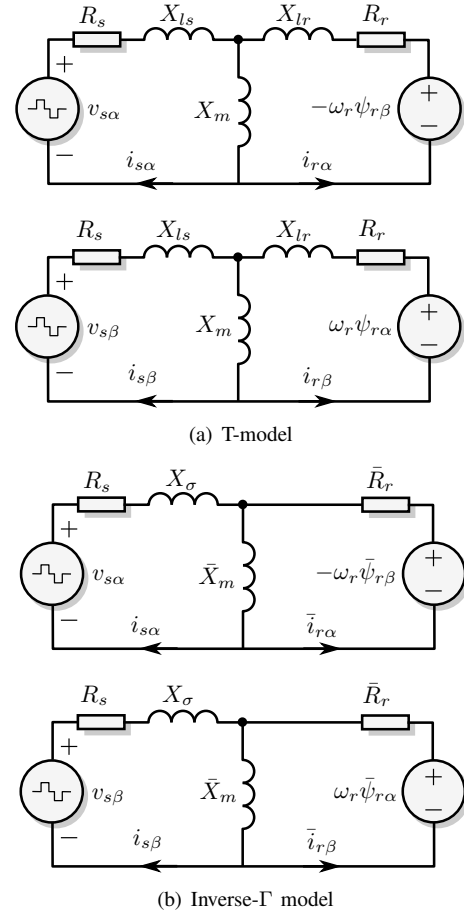


(a) T-model



(b) Inverse-Γ model

Fig. 2: Equivalent models of an IM.

state-space model can be derived by applying circuit analysis to the inverse-Γ model in Fig. 2(b), i.e.,

$$\frac{\mathrm{d}\boldsymbol{x}(t)}{\mathrm{d}t} = \mathbf{F}\boldsymbol{x}(t) + \mathbf{G}\boldsymbol{u}_{abc}(t) \qquad (4a)$$
$$\boldsymbol{y}(t) = \mathbf{C}\boldsymbol{x}(t), \qquad (4b)$$

where $\mathbf{F} \in \mathbb{R}^{4 \times 4}$ is the dynamics matrix

$$\mathbf{F} = \begin{bmatrix} -\frac{1}{\tau_{s,\Gamma}} & -\omega_r & \frac{\bar{R}_r}{X_\sigma \bar{X}_m} & \frac{\omega_r}{X_\sigma} \\ \omega_r & -\frac{1}{\tau_{s,\Gamma}} & -\frac{\omega_r}{X_\sigma} & \frac{\bar{R}_r}{X_\sigma \bar{X}_m} \\ -R_s & 0 & 0 & 0 \\ 0 & -R_s & 0 & 0 \end{bmatrix},$$

with $\omega_r$ being the rotor angular speed, and $\tau_{s,\Gamma}$ the transient stator time constant given by

$$\frac{1}{\tau_{s,\Gamma}} = \frac{\bar{R}_r}{\bar{X}_m} + \frac{\bar{R}_r + R_s}{X_\sigma}.$$

Moreover, the input $\mathbf{G} \in \mathbb{R}^{4 \times 3}$ and output $\mathbf{C} \in \mathbb{R}^{2 \times 4}$ matrices are

$$\mathbf{G} = \frac{V_{\text{dc}}}{2X_\sigma} \begin{bmatrix} \boldsymbol{I}_2 & \boldsymbol{0}_{2 \times 2} \end{bmatrix}^T \boldsymbol{K}, \qquad \mathbf{C} = \begin{bmatrix} \boldsymbol{I}_2 & \boldsymbol{0}_{2 \times 2} \end{bmatrix},$$

where $\boldsymbol{I}$ and $\boldsymbol{0}$ are the identity and zero matrices, respectively, the dimensions of which are indicated by the corresponding subscripts.

Note that the state $\boldsymbol{x}$ in (4) does not explicitly depend on the leakage rotor reactance $X_{lr}$ incorporated in the $\gamma$ coefficient since, as mentioned, the stator current and flux are the same in both models. This greatly benefits the design of the parameter estimation algorithm in Section V, since knowledge of $X_{lr}$ is not required. Finally, to derive the prediction model for the FCS-MPC algorithm, (4) is discretized with the sampling interval $T_s$. To this end, the forward Euler discretization is used, yielding

$$\boldsymbol{x}(k+1) = \mathbf{A}\boldsymbol{x}(k) + \mathbf{B}\boldsymbol{u}_{abc}(k) \tag{5a}$$

$$\boldsymbol{y}(k) = \mathbf{C}\boldsymbol{x}(k), \tag{5b}$$

where $\mathbf{A} = \boldsymbol{I}_4 + \mathbf{F}T_s$, and $\mathbf{B} = \mathbf{G}T_s$ [11].

## III. CONTROLLER DESIGN

In this section the formulation of the optimization problem underlying FCS-MPC is presented. Moreover, the effectiveness of the proposed objective function is assessed in terms of the product of the produced stator current distortions and the switching frequency.

### A. Optimization Problem

The first aim of the controller is to track the stator current reference $\boldsymbol{i}_{s,\mathrm{ref}}$, i.e., to minimize the tracking error $\boldsymbol{i}_{s,\mathrm{err}} = \boldsymbol{i}_{s,\mathrm{ref}} - \boldsymbol{i}_s$. The second control objective relates to the minimization of the switching frequency, i.e., of the control effort $\Delta\boldsymbol{u}_{abc}(\ell) = \boldsymbol{u}_{abc}(\ell) - \boldsymbol{u}_{abc}(\ell-1)$. The former objective relates to the current distortions, which have to be kept low for reduced thermal losses and electromagnetic torque ripple, while the latter to the switching power losses, which for an MV drive have to be as low as possible. These objectives are captured in the following objective function

$$J = \sum_{\ell=k}^{k+N_p-1} \|\boldsymbol{i}_{s,\mathrm{err}}(\ell+1)\|_2^2 + \lambda_u \sum_{\ell=k}^{k+N_c-1} \|\Delta\boldsymbol{u}_{abc}(\ell)\|_2^2, \tag{6}$$

where $\lambda_u > 0$ sets the trade-off between the two terms of (6), i.e., the current distortions and the switching frequency. Moreover, $N_p$ denotes the prediction horizon, i.e., the time window within which the future current trajectories are computed, and $N_c$ is the control horizon, i.e., the time window within which the possible future control actions are evaluated.

An important advantage of the proposed formulation of the objective function (6) is that the $\ell_2$-norm is used, i.e., (6) is a quadratic function. Considering that the drive system in question can be represented as a linear system with integer inputs (see (5)), the adopted design ensures closed-loop (practical) asymptotic stability of the proposed direct MPC algorithm regardless of the value of $\lambda_u$ [27], [28].[3]

The controller utilizes the recursive exhaustive search in Algorithm 1 to find the *optimal* sequence of control actions

$$\boldsymbol{U}^*(k) = \left[\boldsymbol{u}_{abc}^{*T}(k)\ \boldsymbol{u}_{abc}^{*T}(k+1)\ \dots\ \boldsymbol{u}_{abc}^{*T}(k+N_c-1)\right]^T$$

[3]For more information on practical stability of quadratic MPC with integer input, the reader is referred to [29] and references therein.

---

**Algorithm 1** $[J^*,\ \boldsymbol{U}^*] = \mathrm{EXSCH}(\,i,\ \boldsymbol{u}_{abc},\ \boldsymbol{x},\ \boldsymbol{i}_{s,\mathrm{ref}}\,)$

**find** the feasible set for the $(k+i)^{\mathrm{th}}$ prediction step $\boldsymbol{\mathcal{U}}(k+i-1)$
**for all** $\boldsymbol{u}_{abc} \in \boldsymbol{\mathcal{U}}(k+i-1)$ **do**
    **predict** $\boldsymbol{x}(k+i)$ (5) and **compute** $J(k+i)$ (6)
    **if** $i < N_p$ **then**
        **repeat** EXSCH for the next prediction step $i+1$:
        $[J(k+i+1),\ \boldsymbol{U}(k+i)] =$
        $\mathrm{EXSCH}(i{+}1, \boldsymbol{u}_{abc}(k{+}i{-}1), \boldsymbol{x}(k{+}i), \boldsymbol{i}_{s,\mathrm{ref}}(k{+}i{+}1))$
        **add up** the cost from the next prediction step:
        $J(k+i) = J(k+i) + J(k+i+1)$
    **end if**
    find the minimum cost $J(k+i)$ and store the switching
    sequence $\boldsymbol{U}(k+i-1) = [\boldsymbol{u}_{abc}^T(k+i-1)\ \boldsymbol{U}^T(k+i)]^T$
**end for**
$J^* = J(k+i),\ \boldsymbol{U}^* = \boldsymbol{U}(k+i-1)$

---

by solving the following optimization problem

$$\underset{\boldsymbol{U}(k)\in\mathbb{U}}{\mathrm{minimize}}\ J(k) \tag{7a}$$

$$\text{subject to}\ \ \boldsymbol{x}(j+1) = \mathbf{A}\boldsymbol{x}(j) + \mathbf{B}\boldsymbol{u}_{abc}(j) \tag{7b}$$

$$\boldsymbol{y}(j+1) = \mathbf{C}\boldsymbol{x}(j+1), \forall j = k, \dots, k+N_p-1 \tag{7c}$$

$$\|\Delta\boldsymbol{u}(\ell)\|_\infty \le 1, \qquad \forall \ell = k, \dots, k+N_c-1, \tag{7d}$$

where $\mathbb{U} = \boldsymbol{\mathcal{U}} \times \cdots \times \boldsymbol{\mathcal{U}}$ is the $3N_c$-times Cartesian product of the set $\boldsymbol{\mathcal{U}}$, and represents the feasible input set. Note that the initial values of the arguments in Algorithm 1 are $i \leftarrow 1$, $\boldsymbol{u}_{abc} \leftarrow \boldsymbol{u}_{abc}(k-1)$, $\boldsymbol{x} \leftarrow \boldsymbol{x}(k)$, and $\boldsymbol{i}_{s,\mathrm{ref}} \leftarrow \boldsymbol{i}_{s,\mathrm{ref}}(k+1)$.

Problem (7) is typically solved by evaluating all possible solutions, i.e., $3^{3N_c}$, to conclude to the one that results in the minimum value of (6), i.e., the minimum current error and switching effort. Doing this, however, in real time within a few microseconds can be computationally intractable. To keep the computational complexity low, we propose to use two different horizons, i.e., $N_c < N_p$. This approach is in contrast to FCS-MPC implementations where $N_p = N_c$, see [3] and references therein, and it is tailored to the needs of MV drive systems. Specifically, due to the targeted low switching frequencies, only a few changes in the control action are anticipated within the prediction horizon. Thus, for operating at low $f_{\mathrm{sw}}$ the calculation of possible changes in the control action along the whole prediction horizon $N_p$ can be redundant. In addition, by considering that the first steps of the horizon are of more interest since—according to the receding horizon policy [24]—only $\boldsymbol{u}_{abc}^*(k)$ is applied to the inverter, keeping the same control action for the last $N_p - N_c$ steps of the prediction horizon will not adversely affect the system performance. The latter, however, has to be ensured by carefully choosing the prediction window $N_p \cdot T_s$; this point is further elucidated and examined in Section III-B.

Hence, by successfully addressing the aforementioned remarks, the proposed approach can still achieve a favorable performance of the drive (since the prediction horizon $N_p$ remains sufficiently long). Moreover, the complexity of the

optimization problem underlying long-horizon FCS-MPC remains reasonable (since the control horizon $N_c$ can be kept relatively short), rendering its real-time implementation feasible. Finally, it is worth mentioning that if a further reduction of the computational burden of the MPC problem is required, more sophisticated solving methods, e.g., the sphere decoder [6], [30], can be employed.

### B. Assessment of the Objective Function

To evaluate the performance of the proposed objective function (6) with the drive system shown in Fig. 1 and parameters provided in Table I,[4] a set of steady-state simulations was run for different values of $\lambda_u$, such that different switching frequencies $f_{\text{sw}}$ resulted. Each simulation has a duration of 20 fundamental periods, while the sampling interval used is $T_s = 30\,\mu\text{s}$. For each test (i.e., switching frequency $f_{\text{sw}}$), the current total harmonic distortion (THD) $I_{\text{THD}}$ is recorded. In doing so, the product of $I_{\text{THD}}$ and $f_{\text{sw}}$ is computed to serve as a performance metric, i.e.,

$$c_f = I_{\text{THD}} \cdot f_{\text{sw}}. \tag{8}$$

This metric quantifies the quality of the proposed FCS-MPC method as it (approximately) defines a hyperbolic trade-off between $I_{\text{THD}}$ and $f_{\text{sw}}$. This implies that a lower value of $c_f$ indicates a favorable steady-state performance. In the following figures the trends of $c_f$ over a range of switching frequencies are approximated using polynomials for a clear representation of the results.

Given the above framework, the performance metric $c_f$ is shown in Fig. 3 for FCS-MPC with seven different horizon combinations $N = \{N_p, N_c\}$ and nominal parameters in the prediction model. Based on the presented results some noteworthy observations can be made. First, it is evident that, as also reported in [3] and [5], a long horizon improves the drive performance, even if in some cases this seems to be marginal. The reason for this is that the drive system is in essence a first-order system with simple dynamics. Hence, as reported in [3, Section VI-A], very long horizons offer mostly modest performance benefits over a limited range of operating points and switching frequencies, implying that a horizon of a few steps typically suffices to achieve superior performance.

On the other hand, it can be observed that combinations of a very long prediction horizon $N_p$ with a short control horizon $N_c$ can compromise the performance as the switching frequency increases, see, e.g., the trend for $N = \{10, 4\}$ and $N = \{10, 2\}$ for $f_{\text{sw}} > 300\,\text{Hz}$ in Fig. 3(b). Hence, the proposed approach—according to which prediction and control horizons of different length can be used—cannot be directly employed for high $f_{\text{sw}}$.

However, Fig. 3(a) shows that for shorter prediction horizons $N_p$ the critical switching frequency $f_{\text{sw}}^{\text{crit}}$, where the performance starts to deteriorate, is relatively high, e.g., $f_{\text{sw}}^{\text{crit}} \approx 500\,\text{Hz}$ for the combination $N = \{5, 1\}$. The higher
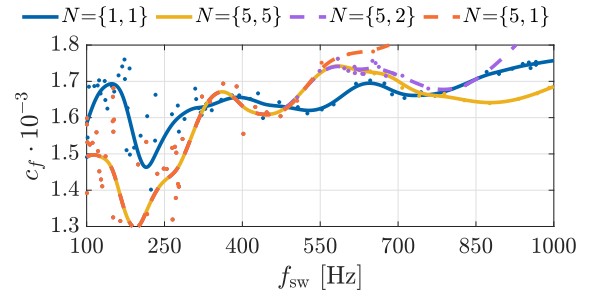
(a) Full range of studied $f_{\text{sw}}$ for $N = \{1, 1\}$, $\{5, 5\}$, $\{5, 2\}$, and $\{5, 1\}$.
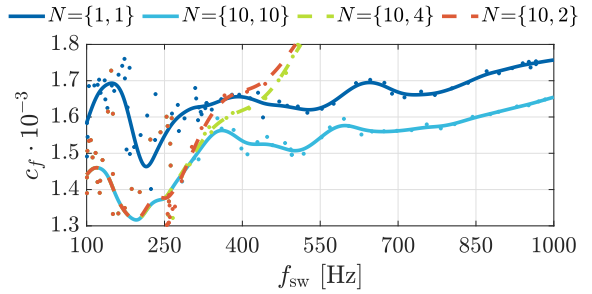


(b) Full range of studied $f_{\text{sw}}$ for $N = \{1, 1\}$, $\{10, 10\}$, $\{10, 4\}$, and $\{10, 2\}$.

Fig. 3: Performance metric $c_f$ as a function of the switching frequency $f_{\text{sw}}$ for horizon combinations $N = \{1, 1\}$, $\{5, 5\}$, $\{5, 2\}$, $\{5, 1\}$, $\{10, 10\}$, $\{10, 4\}$ and $\{10, 2\}$.

$f_{\text{sw}}^{\text{crit}}$ is explained by the shorter prediction horizon $N_p$ and, consequently, lower number of anticipated changes in the control action within $N_p$, as mentioned in Section III-A. An important remark is that FCS-MPC with the horizon combination $N = \{5, 1\}$ achieves the exact same steady-state performance—in terms of $c_f$—with $N = \{5, 5\}$ for up to $f_{\text{sw}} = 500\,\text{Hz}$. Hence, it can be deduced that long-horizon FCS-MPC with the proposed objective function (6) fully utilizes the advantages associated with long horizons, see [3, Section VI]. Finally, it is important to point out that for the relevant range of switching frequencies for MV VSD systems, i.e., $f_{\text{sw}} < 500\,\text{Hz}$, it can be seen that FCS-MPC with $N_p = 5$ achieves similar—and occasionally even better (e.g., for $f_{\text{sw}} > 400\,\text{Hz}$)—values of $c_f$ compared with FCS-MPC with $N_p = 10$ and short control horizons $N_c$. Thus, it can be concluded that for the switching frequency range of interest the horizon combination $N = \{5, 1\}$ is a favorable one to achieve the desired performance benefits without increasing the computational complexity of the problem.

Besides the examined simulation results, the choice of $N$ can be verified by the calculation of the critical switching frequency $f_{\text{sw}}^{\text{crit}}$. Since for the chosen $N$ the drive operates within the desired range of switching frequencies when only one switching transition occurs in the prediction window $N_p \cdot T_s$, a boundary condition for the prediction horizon steps is

$$N_p \cdot T_s = (12 f_{\text{sw}}^{\text{crit}})^{-1}, \tag{9}$$

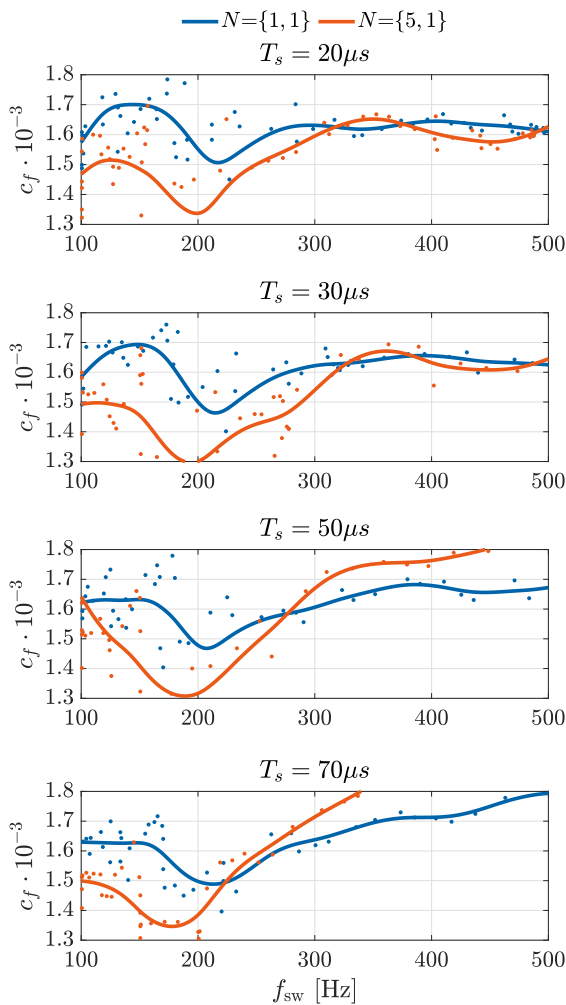where a three-level converter with 12 semiconductor devices

Fig. 4: Performance metric $c_f$ as a function of the switching frequency $f_{sw}$ for horizon combinations $N = \{1, 1\}$ and $\{5, 1\}$ with different sampling intervals $T_s$.
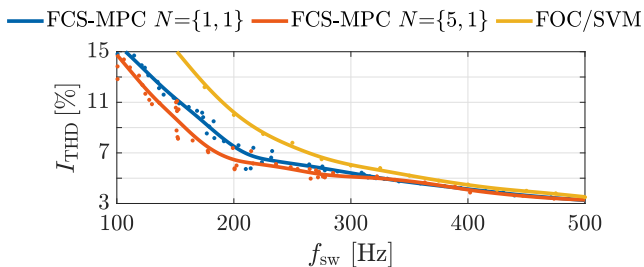


Fig. 5: Trade-off between current THD $I_{THD}$ and switching frequency $f_{sw}$ for FCS-MPC with horizon combinations $N = \{1, 1\}$ and $\{5, 1\}$ for $T_s = 30\,\mu s$, and for FOC with SVM.

is considered. The right-hand side of (9) indicates the average time between two consecutive switching transitions [12]. Solving (9) for $f_{sw}^{crit}$ with $N_p = 5$ and $T_s = 30\,\mu s$ yields $f_{sw}^{crit} = 555$ Hz. This value of $f_{sw}^{crit}$ can also be devised from the results presented in Fig. 3(a). Thus, for a given system with a specific $T_s$ and operating range of $f_{sw}$ the maximum $N_p$ can be calculated using (9) and then verified by simulations. Nevertheless, it should be mentioned that this

approach is tailored to applications where a low switching frequency is desired, e.g., MV drives. For other applications, such as low-voltage systems that typically operate at much higher switching frequencies $f_{sw}$, setting $N_p = N_c$ is a more reasonable choice as (9) yields a very small value for $N_p$.

To further assess the objective function and the relevant design choices, the effect of the sampling interval $T_s$ is examined. To this aim, the performance metric $c_f$ is studied for different sampling intervals. Fig. 4 demonstrates the performance metric for two horizon combinations and four different values of the sampling interval. As can be seen, $c_f$ increases with an increasing sampling interval, indicating a performance deterioration. It is noteworthy, that such an adverse effect is more prominent when the combination $N = \{5, 1\}$ is used. This implies that a short sampling interval is preferable, as it better realizes the performance advantages of long-horizon FCS-MPC. However, as can be observed, the difference in $c_f$ between $T_s = 20\,\mu s$ and $T_s = 30\,\mu s$ is marginal for the given range of $f_{sw}$.

The presented observations are in line with the guidelines regarding the granularity of switching for FCS-MPC methods. As highlighted in [3, Section V], the desired sampling-to-switching frequency ratio should be close to 100 so that a favorable steady-state operation is achieved. This trend is indeed demonstrated in Figs. 3 and 4, where the performance deteriorates as the switching frequency increases due to the decreasing granularity of switching.

Given the above analysis, and since the target switching frequency range is below 500 Hz, only horizon combinations $N = \{5, 1\}$ and $N = \{1, 1\}$ with sampling interval $T_s = 30\,\mu s$ are analyzed and compared in the following sections. Fig. 5 shows the trade-off curve between $I_{THD}$ and $f_{sw}$ for the proposed approach with the chosen design parameters. As can be seen, the proposed FCS-MPC scheme can improve the current THD by around 10% at low switching frequencies compared to one-step FCS-MPC. Notably, this improvement comes at a minor computational cost, since the size of the five-step FCS-MPC optimization problem is very small as the number of candidate solutions is the same to that of one-step FCS-MPC.

Finally, for comparison purposes, the standard industrial solution for MV drives, namely field oriented control (FOC) with space vector modulation (SVM), is used for benchmarking purposes. The associated trade-off curve between $I_{THD}$ and $f_{sw}$ is also shown in Fig. 5. As can be seen, both FCS-MPC formulations outperform FOC/SVM at low switching frequencies, i.e., at the relevant range of $f_{sw}$ for MV drives. Such a favorable behavior can be attributed to the beneficial formulation of the MPC problem [3].

## IV. Robustness Analysis

Depending on the motor operating point, its parameters can vary considerably, e.g., as a function of the motor temperature for resistances, or under the effect of magnetic saturation for reactances. To identify the most important parameters for an estimation algorithm design, the effect of the parameter
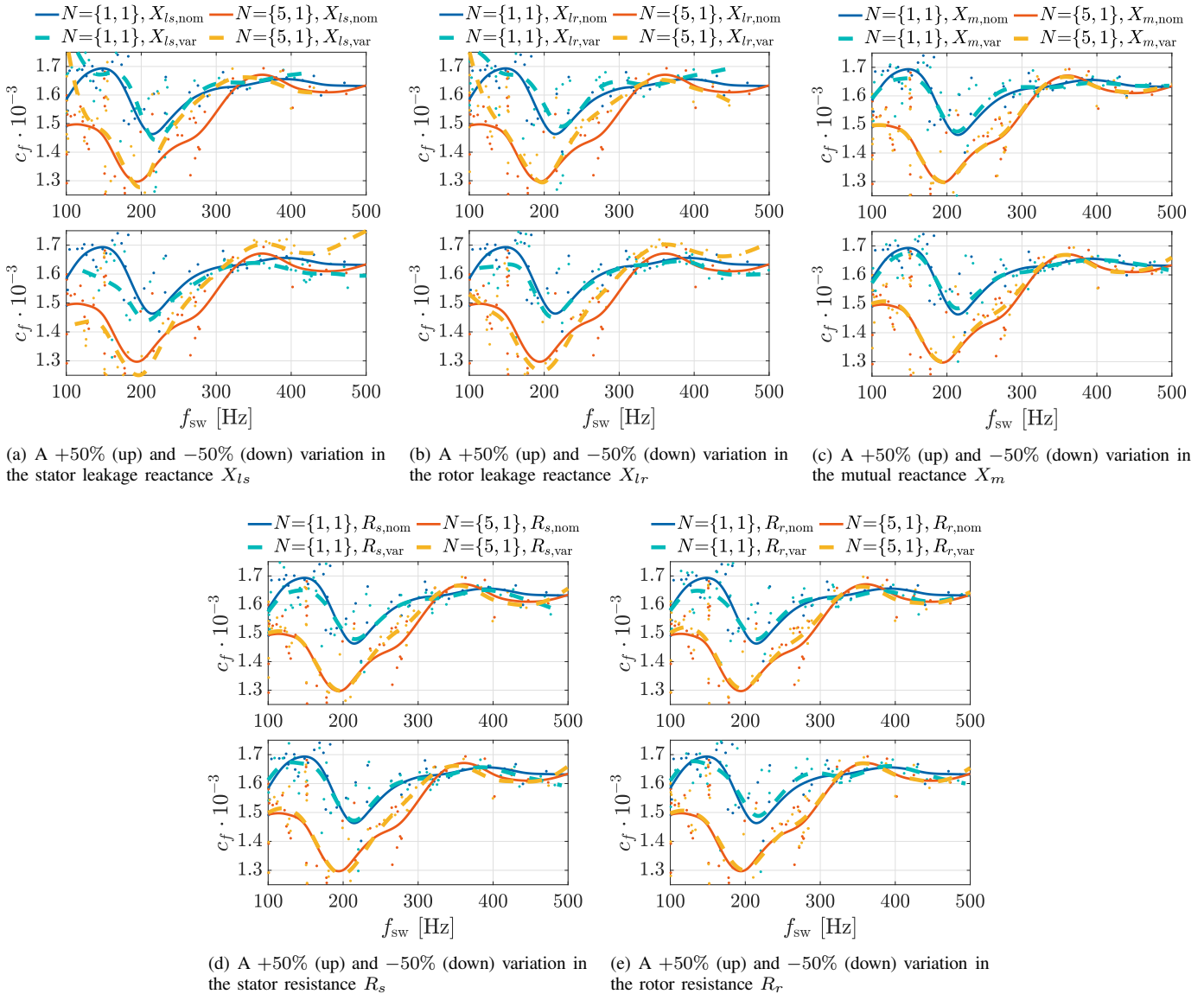
(a) A $+50\%$ (up) and $-50\%$ (down) variation in the stator leakage reactance $X_{ls}$

(b) A $+50\%$ (up) and $-50\%$ (down) variation in the rotor leakage reactance $X_{lr}$

(c) A $+50\%$ (up) and $-50\%$ (down) variation in the mutual reactance $X_m$

(d) A $+50\%$ (up) and $-50\%$ (down) variation in the stator resistance $R_s$

(e) A $+50\%$ (up) and $-50\%$ (down) variation in the rotor resistance $R_r$

Fig. 6: Performance metric $c_f$ as a function of the switching frequency $f_{\text{sw}}$ for horizon combinations $N=\{1,1\}$ and $\{5,1\}$.

mismatches in the prediction model on the performance metric $c_f$ of the proposed FCS-MPC is examined. To this aim, $\pm 50\%$ variations in $X_{ls}$, $X_{lr}$, $X_m$, $R_s$, and $R_r$ are studied for the chosen horizon combinations and the same values of $\lambda_u$ used in Section III. Note that for all simulations operation of the IM at the rated speed and torque is assumed.

The results in Figs. 6(a), 6(b) and 6(c) show that, regardless of the horizon combination, variations in $X_{ls}$ and $X_{lr}$ clearly detract from the controller performance metric, whereas mismatches in $X_m$ change it only slightly. Moreover, it is seen that underestimated reactances lead to more substantial performance deviations from the nominal behavior. On the other hand, as shown in Figs. 6(d) and 6(e), variations in the stator and rotor resistances have a negligible effect on the performance metric $c_f$, mainly due to their typically very small value in MV drives.

The presented results are reasonable since an IM can be considered as a load with essentially inductive behavior, where

the reactances can be modeled by the total leakage reactance $X_\sigma$, see (3c). Note that the latter is mainly sensitive to deviations in the stator and rotor leakage reactances, see [31]. Hence, it can be concluded that the mutual reactance as well as the stator and rotor resistances can be excluded from consideration when designing the estimation algorithm. On the other hand, the FCS-MPC robustness can be significantly improved by correctly estimating $X_{lr}$ and $X_{ls}$, and updating the prediction model accordingly. However, as mentioned in Section II, owing to the adopted inverse-$\Gamma$ model, only the total leakage reactance $X_\sigma$ needs to be accurately estimated to address the adverse effects of mismatches in $X_{ls}$ and $X_{lr}$. The estimation algorithm developed in Section V exploits this fact.

## V. ESTIMATOR DESIGN

Motivated by the robustness analysis results, a simple estimation method is introduced in the following. By assuming

replacements
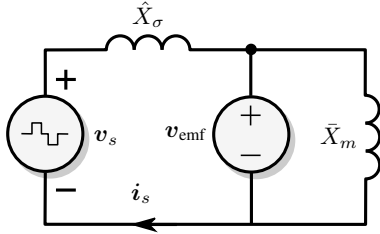


(a) Simplified equivalent model of an IM
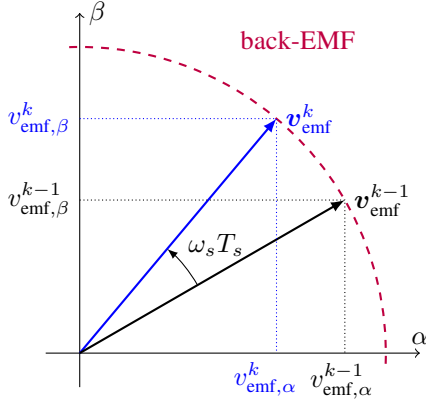


(b) Representation of the back-EMF

Fig. 7: Principle of the proposed estimation algorithm.

that the stator $R_s$ and rotor $R_r$ resistances are approximately zero—which is a valid assumption for MV machines [24]—the inverse-$\Gamma$-equivalent model in Fig. 2(b) can be represented as in Fig. 7(a), where $\boldsymbol{v}_{\mathrm{emf}}$ is the back electromotive force (back-EMF). The differential equation that describes the dynamics of the stator current is

$$\hat{X}_\sigma \frac{\mathrm{d}\boldsymbol{i}_s(t)}{\mathrm{d}t} = \boldsymbol{v}_s(t) - \boldsymbol{v}_{\mathrm{emf}}(t), \tag{10}$$

where $\hat{X}_\sigma$ denotes the total leakage reactance value to be estimated and used in the prediction model (5).

The estimation algorithm is based on the assumption that the back-EMF is sinusoidal and its amplitude remains constant during the sampling interval $T_s$, see Fig. 7(b). Given this, the total leakage reactance $\hat{X}_\sigma$ can be devised from

$$\|\boldsymbol{v}_{\mathrm{emf}}(k)\|_2^2 - \|\boldsymbol{v}_{\mathrm{emf}}(k-1)\|_2^2 =$$
$$v_{\mathrm{emf},\alpha}^2(k) + v_{\mathrm{emf},\beta}^2(k) - v_{\mathrm{emf},\alpha}^2(k-1) - v_{\mathrm{emf},\beta}^2(k-1) = 0\,. \tag{11}$$

Each term in (11) can be found by discretizing (10) with the forward Euler method, i.e.,

$$v_{\mathrm{emf},z}^2(\ell) = (\hat{X}_\sigma \Delta A_z(\ell+1) + v_{sz}(\ell))^2\,, \tag{12}$$

where

$$\Delta A_z(\ell+1) = -\frac{i_{sz}(\ell+1) - i_{sz}(\ell)}{T_s}\,, \tag{13}$$

**Algorithm 2** Update $X_\sigma^{\mathrm{pred}}$

---

**if** $B = 0$ **or** $4CA/B^2 > 1$ **then**
    $X_\sigma^{\mathrm{pred}} \leftarrow X_\sigma^{\mathrm{pred}}(k-1)$
    **return**
**end if**
calculate $\hat{X}_{\sigma 1,2}$ from (17) and $|\varphi_{\sigma,l} - \varphi|$ with (19)
$\Delta\varphi = \infty$
**for** $l \in \{1, 2, 3\}$ **do**
    **if** $|\varphi_{\sigma,l} - \varphi| < \Delta\varphi$ **then**
        $\Delta\varphi = |\varphi_{\sigma,l} - \varphi|$
        $i \leftarrow l$
    **end if**
**end for**
$X_\sigma^{\mathrm{pred}} \leftarrow \hat{X}_{\sigma,i}$

---

with $z \in \{\alpha, \beta\}$, and $\ell \in \{k, k-1\}$. For example, for $z = \alpha$ and $\ell = k-1$, $v_{\mathrm{emf},\alpha}(k-1)$ is calculated as

$$v_{\mathrm{emf},\alpha}^2(k-1) =$$
$$\left(-\hat{X}_\sigma \cdot \frac{i_{s\alpha}(k) - i_{s\alpha}(k-1)}{T_s} + v_{s\alpha}(k-1)\right)^2\,. \tag{14}$$

With the help of (12) and (13), (11) can be written in the form of the following quadratic equation [32]

$$\hat{X}_\sigma^2 A + \hat{X}_\sigma B + C = 0\,, \tag{15}$$

where

$$A = \Delta A_\alpha^2(k+1) + \Delta A_\beta^2(k+1) - \Delta A_\alpha^2(k)$$
$$\qquad - \Delta A_\beta^2(k)\,, \tag{16a}$$
$$B = 2\Big(\Delta A_\alpha(k+1)v_{s\alpha}(k) + \Delta A_\beta(k+1)v_{s\beta}(k)$$
$$\qquad - \Delta A_\alpha(k)v_{s\alpha}(k-1) - \Delta A_\beta(k)v_{s\beta}(k-1)\Big)\,, \tag{16b}$$
$$C = v_{s\alpha}^2(k) + v_{s\beta}^2(k) - v_{s\alpha}^2(k-1) - v_{s\beta}^2(k-1)\,. \tag{16c}$$

After substituting (16) into (15), the total leakage reactance is calculated with

$$\hat{X}_{\sigma 1,2} = \frac{B}{2A}\left[-1 \pm \sqrt{1 - \frac{4CA}{B^2}}\right]\,, \tag{17}$$

where the meaningful root is kept. The criterion for the latter is based on the assumption that the back-EMF vector $\boldsymbol{v}_{\mathrm{emf}}$ rotates counterclockwise by the angle corresponding to one sampling interval when the correct value of $\hat{X}_\sigma$ is used, i.e.,

$$\varphi = \omega_s T_s\,, \tag{18}$$

with $\omega_s$ being the stator angular speed.

To implement the root-choosing criterion for (17), the three possible angles between the back-EMF vectors at two consecutive sampling intervals—$\boldsymbol{v}_{\mathrm{emf}}(k-1)$ and $\boldsymbol{v}_{\mathrm{emf}}(k)$—are calculated with

$$\varphi_{\sigma,l} = \arccos\left(\frac{\boldsymbol{v}_{\mathrm{emf},l}(k)^T \boldsymbol{v}_{\mathrm{emf},l}(k-1)}{\|\boldsymbol{v}_{\mathrm{emf},l}(k)\|_2 \|\boldsymbol{v}_{\mathrm{emf},l}(k-1)\|_2}\right)\,, \tag{19}$$
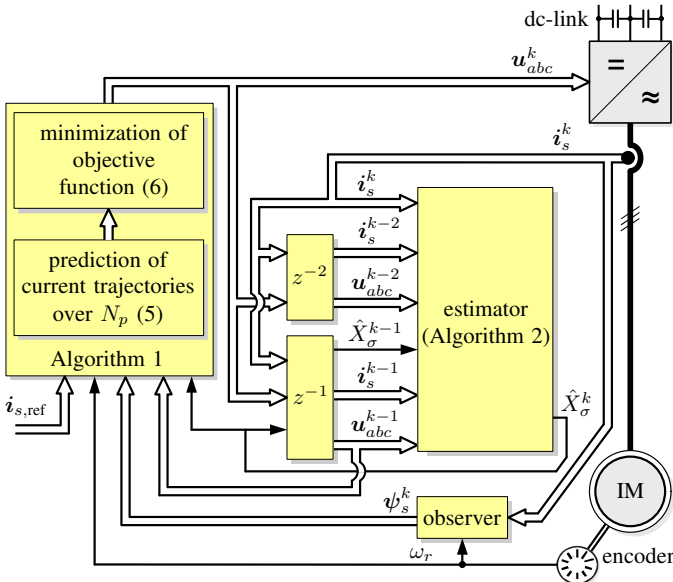
Fig. 8: Direct model predictive control with reference tracking and total leakage reactance estimator for MV VSD systems.



Fig. 9: Instantaneous estimated value $\hat{X}_\sigma$ and its value based on the moving average, i.e., $\overline{X}_\sigma$, while applying a mismatch (up) and a zoomed-in view (down). A variation of $-50\%$ is simultaneously introduced in both $X_{ls}$ and $X_{lr}$ at 0.2 s, resulting in the wrong value of $X_\sigma^{\text{pred}} = 0.13$ p.u., whereas the actual machine reactance is $X_\sigma^{\text{mach}} = 0.2548$ p.u.. The FCS-MPC uses the wrong value of $X_\sigma^{\text{pred}}$ up until 1.4 s, i.e., the estimator is bypassed. At 1.4 s the estimator is utilized and the correct value is provided to the controller, i.e., $X_\sigma^{\text{pred}} = \overline{X}_\sigma$.



Fig. 10: The normalized histogram and the posterior predictive probability distribution of the $\hat{X}_\sigma$ values recorded over a span of 10 s. The 95 % confidence interval for the next estimation is $\text{CI}_{95} = [0.247, 0.262]$ which is within the range of $\pm 3\%$ from the nominal machine reactance $X_\sigma^{\text{mach}} = 0.2548$ p.u.

where $l \in \{1, 2, 3\}$. Note that in (19), the values of the back-EMF vectors are computed by substituting the two possible values of $\hat{X}_\sigma$, i.e., $\hat{X}_{\sigma 1,2}$, from (17) into (12). Additionally, the third value in (19), i.e., when $l = 3$, corresponds to the total leakage reactance computed at the previous time step, i.e., $\hat{X}_\sigma(k-1)$; this value is substituted into (12) in the same manner. Note that, in theory, (18) and (19) should result in the same angle when the correct value of $\hat{X}_\sigma$ is used. As, however, in practice small deviations may exist, the difference $|\varphi_{\sigma,l} - \varphi|$ is computed and the $\hat{X}_\sigma$ that leads to the smallest one is chosen. The block diagram of the proposed robust FCS-MPC approach is shown in Fig. 8.

Further analysis of (17) reveals supplementary conditions which have to be addressed in order to guarantee feasibility of the estimation algorithm results. Specifically, when a switch position does not change between two consecutive sampling intervals, i.e., $\boldsymbol{u}_{abc}(k) = \boldsymbol{u}_{abc}(k-1)$, (16b) is often equal to zero, thus leading to an incorrect calculation. Additionally, cases where the root in (17) is negative are excluded from consideration in the estimation algorithm.

Altogether, the above-mentioned conditions are summarized in Algorithm 2. In the end, these special considerations force the estimator to be idle, i.e., to use the value of the total leakage reactance from the previous step $X_\sigma^{\text{pred}}(k-1)$ in the prediction model, for the biggest part of the fundamental period, namely around $90\%$ of the time for the chosen value of $T_s$. To visualize this point, the time intervals during which the estimator is not executed are shaded in Fig. 9. Moreover, a simple moving average technique with a time window of ten sampling intervals is employed to improve the accuracy of the estimation and mitigate the measurement noise. In doing so, the averaged value $\overline{X}_\sigma$ of the estimated reactance is computed. It is important to point out that such a moving average may introduce a small delay in the computation of the total leakage
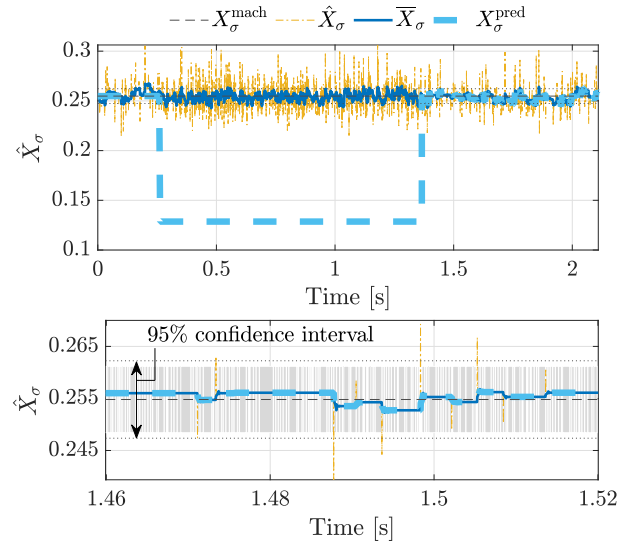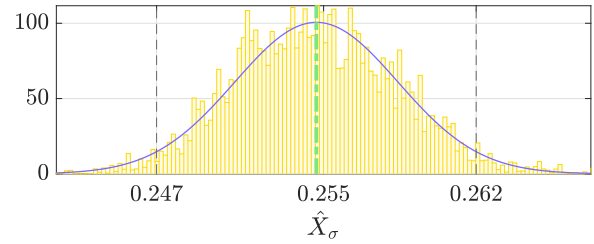
reactance. This small delay, however, is acceptable considering the very small sampling interval $T_s$ and the fact that the total leakage reactance changes slowly over a few $T_s$. This means that the reactance value used in the prediction model $X_\sigma^{\text{pred}}$ does not need to be updated at every iteration of the MPC algorithm, and the estimation algorithm can be executed at a slower rate, if needed.

## VI. ESTIMATOR PERFORMANCE EVALUATION

MV drives with power and voltage ratings as those presented in Table I are not readily available for testing the control software. Hence, to facilitate the development of new control algorithms, while providing a risk-free environment, it is common practice to assess the controller performance in a HIL environment, where the presence of the physical system is not required. Such an approach allows for testing the MV VSD system under both nominal and transient operating conditions.

Given the above, the effectiveness of the proposed control and estimation scheme is demonstrated by the time- and
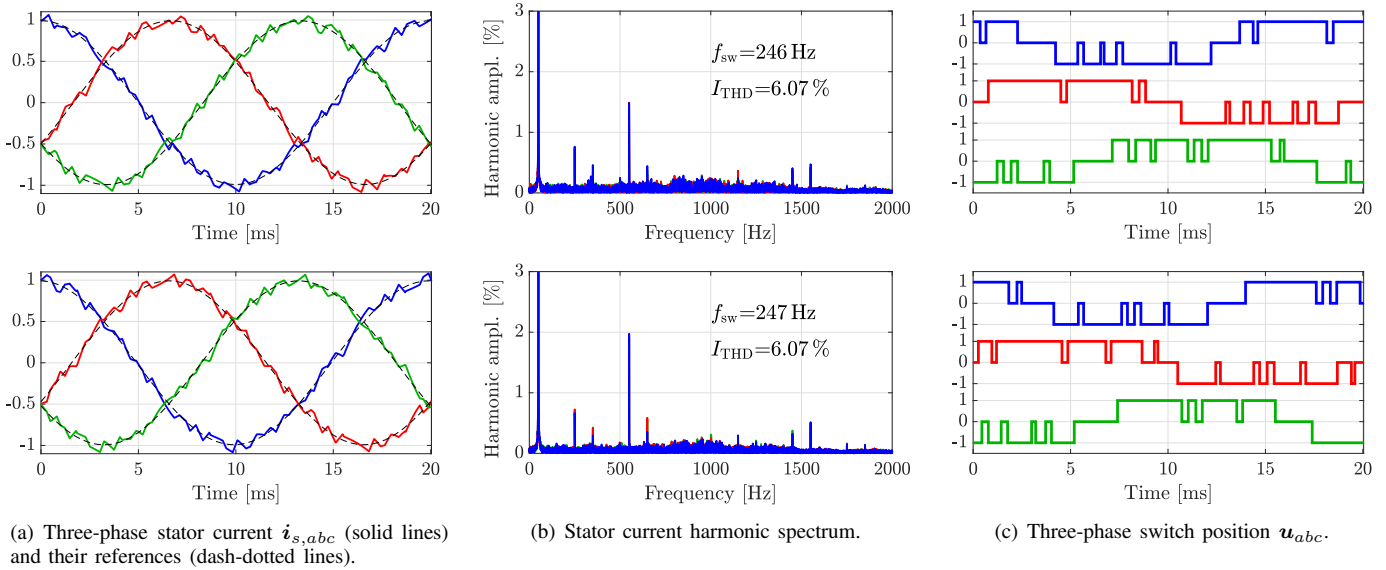
(a) Three-phase stator current $\boldsymbol{i}_{s,abc}$ (solid lines) and their references (dash-dotted lines).

(b) Stator current harmonic spectrum.

(c) Three-phase switch position $\boldsymbol{u}_{abc}$.

Fig. 11: HIL results at steady-state operation with the proposed FCS-MPC for $N = \{5, 1\}$. Top row: nominal parameters. Bottom row: a simultaneous $-50\%$ variation in both $X_{ls}$ and $X_{lr}$ is introduced while the estimation algorithm is active, resulting in effectively the same performance.



(a) Without (left) and with (right) the estimation algorithm.

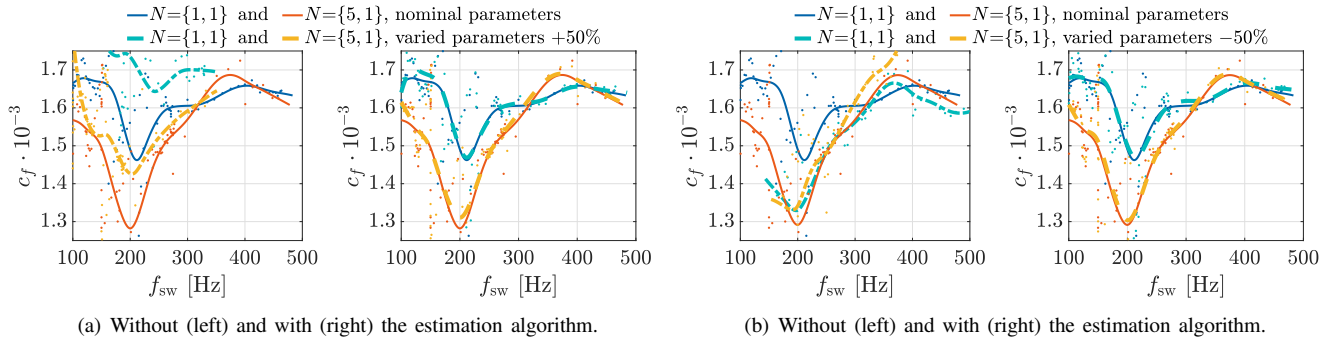(b) Without (left) and with (right) the estimation algorithm.

Fig. 12: HIL results for the performance metric $c_f$ as a function of the switching frequency $f_{sw}$ for horizon combinations $N = \{1, 1\}$ and $\{5, 1\}$. A simultaneous $+50\%$ variation in both $X_{ls}$ and $X_{lr}$ is introduced in Fig. 12(a), whereas a simultaneous $-50\%$ variation is introduced in Fig. 12(b) for the same reactances. Each individual HIL test—indicated by a dot—corresponds to a real-time simulation of $2\,\text{s}$.

frequency-domain results from the tests conducted on the HIL setup. The HIL system is based on a PLECS RT-Box 1 real-time system that employs a Xilinx Z-7030 system-on-chip technology with an FPGA and two embedded CPU cores. The MV VSD system is simulated at a sampling interval of $2.5\,\mu\text{s}$ on the processor of the PLECS RT-Box 1, while the FPGA is used for the data acquisition (DAQ) to ensure high fidelity of the real-time simulation. The measurements acquired from the VSD system are fed to the control platform described below via an analog interface, while the switch positions are received by the inverter via digital inputs. For more details on the HIL setup, the reader is referred to [33].

The proposed controller and estimation schemes are implemented on the dSPACE SCALEXIO system, which has a $2.8\,\text{GHz}$ Intel i7-6820EQ processor and a Xilinx Kintex-7 FPGA. Both the control and estimation loops are implemented on the processor, while the FPGA performs the DAQ. The tests performed relate to the VSD system shown in Fig. 1, with the parameters in Table I, while $N = \{5, 1\}$ and $T_s = 30\,\mu\text{s}$ are

chosen. All results in this section are shown in the p.u. system. By simultaneously varying both leakage reactances, $X_{ls}$ and $X_{lr}$ by $\pm 50\%$, variations of approximately $\pm 50\%$ in the total leakage reactance $X_\sigma$ are introduced [31].

### A. Steady-State Operation

Fig. 9 shows that in the presence of the mentioned mismatches, the proposed estimation scheme manages to estimate the correct value of $X_\sigma$, update the prediction model accordingly, and, thus, ensure that the FCS-MPC will remain robust to variations in the leakage reactances. Notably, the instantaneous value $\hat{X}_\sigma$ (see the yellow dash-dotted line) exhibits occasional spikes. These are due to the fact that the estimation scheme relies on the stator current derivatives (see (10)). As a result, the instantaneous estimations can be adversely affected by noise. Nevertheless, as mentioned in Section V, the adopted moving average strategy tackles this issue and provides the averaged value $\overline{X}_\sigma$ which is very close to the actual value of $X_\sigma$.

(a) Steps in the electromagnetic torque.

(b) Three-phase stator current $i_{abc}$.
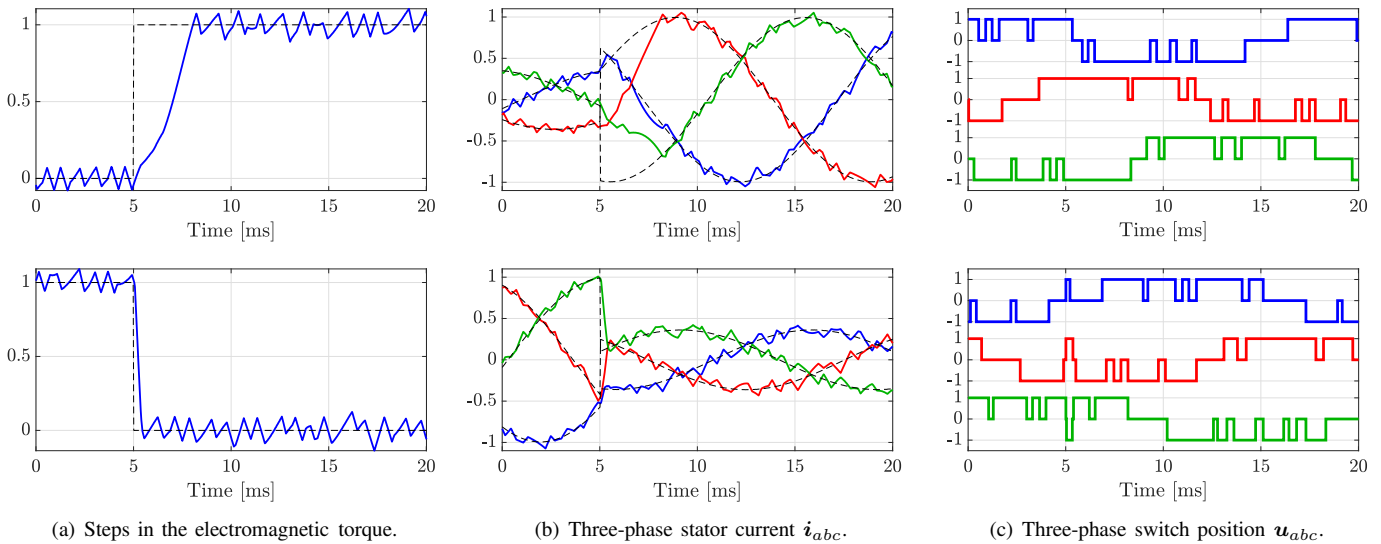
(c) Three-phase switch position $u_{abc}$.

Fig. 13: HIL results during torque reference step changes with the proposed FCS-MPC for $N = \{5, 1\}$. A simultaneous $-50\%$ variation in both $X_{ls}$ and $X_{lr}$ is introduced while the estimation algorithm is *active*. The average switching frequency is $f_{\text{sw}} \approx 250$ Hz.



(a) Steps in the electromagnetic torque.

(b) Three-phase stator current $i_{abc}$.
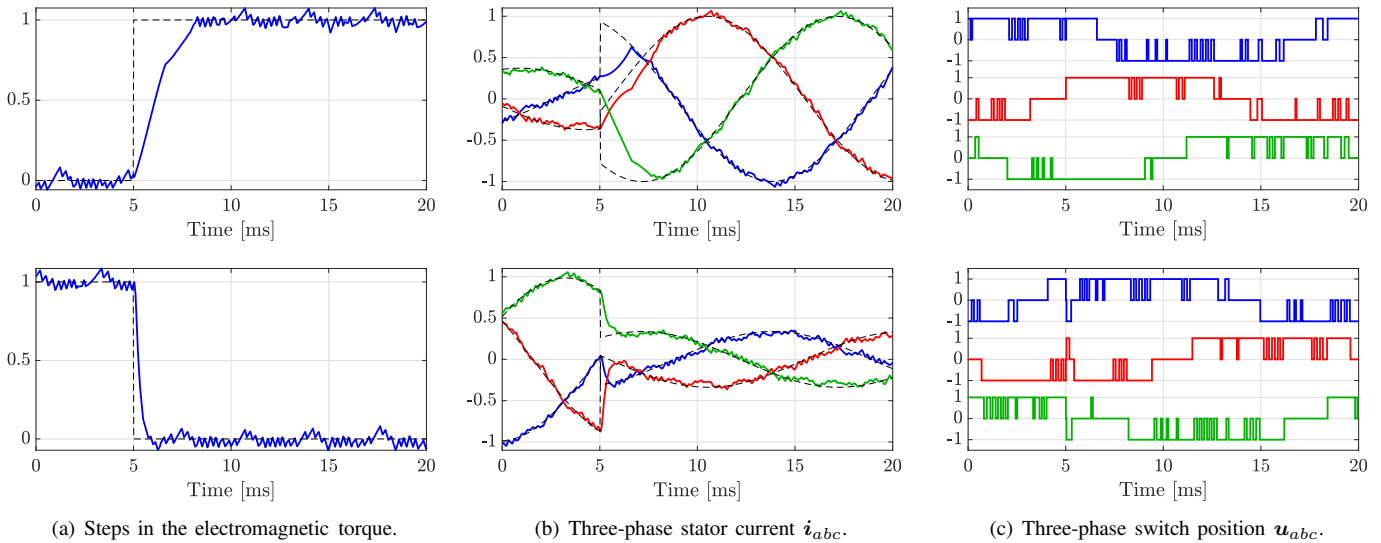
(c) Three-phase switch position $u_{abc}$.

Fig. 14: HIL results during torque reference step changes with the proposed FCS-MPC for $N = \{5, 1\}$. A simultaneous $-50\%$ variation in both $X_{ls}$ and $X_{lr}$ is introduced while the estimation algorithm is *inactive*. The average switching frequency is $f_{\text{sw}} \approx 545$ Hz.

The estimation accuracy can be evaluated from Fig. 10. Therein, it can be seen that in $95\%$ of the cases the estimated value $\hat{X}_\sigma$ is within a range of $\pm 3\%$ from the nominal value of $X_\sigma$, i.e., the estimation accuracy is very high. The time- and frequency-domain results in Fig. 11 provide further insight into the efficacy of the proposed estimation scheme. Specifically, this figure clearly shows that when the estimator is active, such that the estimated value $\hat{X}_\sigma$ is used in the prediction model, the same performance with $f_{\text{sw}} \approx 245$ Hz and $I_{\text{THD}} \approx 6\%$ is achieved regardless of whether there are significant mismatches in the system parameters or not.

As a last test, the advantages of the proposed approach are also highlighted in Fig. 12, which shows how the mismatches detract from the system performance achieved when nominal parameters are considered. It is worth noting that the HIL results in Fig. 12 are similar to the ones obtained from the simulations in Fig. 6. On the other hand, the FCS-MPC scheme performance seems immune to any parameter mismatches when the estimation algorithm is activated regardless of the degree of the said mismatches, see Fig. 12. This figure clearly demonstrates the effectiveness of the proposed estimation algorithm, which, in conjunction with the designed FCS-MPC algorithm, result in a favorable drive behavior. Namely, in line with the simulation results, it can be observed that the long horizon FCS-MPC delivers lower values for the $c_f$ metric, even in the presence of severe parameter mismatches. This is clearly shown in the right-hand side figures of Figs. 12(a) and 12(b), where the dashed orange line overlaps with the red one.

TABLE II: Total average and maximum turnaround time $t_{\text{ta}}$ of the proposed direct MPC scheme (with and without the estimator) for different horizon combinations $N = \{N_p, N_c\}$.

| | $N = \{1, 1\}$ | $N = \{5, 1\}$ | $N = \{5, 1\}$ w/estimator |
|---|---|---|---|
| Average $t_{\text{ta}}$ | $15.5\,\mu\text{s}$ | $19.1\,\mu\text{s}$ | $19.3\,\mu\text{s}$ |
| Maximum $t_{\text{ta}}$ | $18.8\,\mu\text{s}$ | $24.1\,\mu\text{s}$ | $24.6\,\mu\text{s}$ |

### B. Operation During Transients

To verify that the proposed estimation algorithm remains effective during transient operating conditions, its performance is tested when torque reference step changes are applied. Specifically, the transient behavior in the presence of mismatches is shown in Fig. 13, where the electromagnetic torque $T_{\text{el}}$ is changed from $0$ to $1$ p.u. (upper row) and vice versa (lower row) at $t = 5$ ms. It is seen that the stator currents—and consequently the electromagnetic torque—successfully track their reference values. Additionally, the torque does not exhibit any overshoots during the step changes, while the settling times for the step-up and step-down tests are $3.3$ ms and $0.6$ ms, respectively.

These results clearly show that the dynamic performance of the FCS-MPC is excellent as it is only limited by the available voltage, as it is typical with direct control methods. Moreover, the fact that the estimation scheme can provide the correct value of $X_\sigma$ in the prediction model guarantees that the controller behavior does not deteriorate. Finally, it is important to mention that the estimation scheme, and subsequently the FCS-MPC algorithm, do not need to know which leakage reactance is changed and by how much, since, thanks to the adopted modeling, only knowledge of $X_\sigma$ is required. It can be concluded that this provides the proposed controller with a high degree of robustness.

Finally, to study the effect of parameter uncertainties on the dynamic behavior of the system, the same transient scenarios are tested while the estimator is inactive, see Fig. 14. The presented results demonstrate that although the settling times remain unchanged the tracking performance degrades. Moreover, as the controller uses the wrong total leakage reactance, it tends to react faster and more aggressively to the tracking errors. As a result, the average switching frequency increases to about $545$ Hz, see Fig. 14(c).

### C. Computational Burden

To assess the computational burden of the presented algorithm, Table II summarizes the total turnaround time $t_{\text{ta}}$ on the dSPACE platform for the proposed MPC scheme with the two studied horizon combinations, i.e., $N = \{1, 1\}$ and $N = \{5, 1\}$. As can be seen, owing to the proposed formulation of the direct MPC problem, the maximum turnaround time—which is the most relevant metric from a real-time implementation point of view—of the 5-step MPC is greater by only $5.3\,\mu\text{s}$ than that of the traditional one-step FCS-MPC. Moreover, for reasons of completeness, Table II shows the turnaround time when the estimator is activated to demonstrate its small computational requirements. It is worth noting that the computational load of the estimator is independent of the MPC formulation, thus it can be considered as an overhead to the total computational burden of the implemented control scheme.

## VII. CONCLUSIONS

This paper proposed a long-horizon FCS-MPC strategy for IM MV drives that achieves superior steady-state performance compared with the traditional one-step FCS-MPC and the standard industrial control solution, i.e., FOC with SVM. Moreover, thanks to its direct control nature, very short settling times during transients are achieved. In addition to the performance benefits of the proposed control scheme, the two main drawbacks of long-horizon FCS-MPC are also addressed, namely (a) the pronounced computational complexity, and (b) the sensitivity to parameter variations and mismatches. To tackle the first shortcoming, the optimization problem underlying long-horizon FCS-MPC is tailored to the needs of the chosen case study by introducing the concept of separate prediction and control horizons. In doing so, a long prediction horizon can be implemented—and thus the associated performance benefits fully harvested—with only a small computational overhead compared with one-step FCS-MPC. As for the robustness of the proposed long-horizon FCS-MPC, this is improved by implementing an effective and computationally light estimation algorithm tailored to MV drives. The accuracy of the estimation scheme is further enhanced by the adopted modeling of the MV drive, i.e., the so-called inverse-$\Gamma$ model. The presented HIL results based on a three-level NPC inverter driving an MV IM demonstrate the effectiveness of the proposed control and estimation approaches. As shown, a superior drive performance is achieved and maintained, even in the presence of significant variations in the system parameters in comparison to traditional one-step FCS-MPC.

## REFERENCES

[1] A. Tregubov, P. Karamanakos, and L. Ortombina, "A computationally efficient robust direct model predictive control for medium voltage induction motor drives," in *Proc. IEEE Energy Convers. Congr. Expo.*, Vancouver, BC, Canada, Oct. 2021, pp. 4690–4697.

[2] E. Liegmann, T. Schindler, P. Karamanakos, A. Dietz, and R. Kennel, "UltraZohm—An open-source rapid control prototyping platform for power electronic systems," in *Proc. Int. Conf. on Optim. of Elect. and Electron. Equip.*, Brasov, Romania, Sep. 2021, pp. 445–450.

[3] P. Karamanakos and T. Geyer, "Guidelines for the design of finite control set model predictive controllers," *IEEE Trans. Power Electron.*, vol. 35, no. 7, pp. 7434–7450, Jul. 2020.

[4] P. Cortés, M. P. Kazmierkowski, R. M. Kennel, D. E. Quevedo, and J. Rodríguez, "Predictive control in power electronics and drives," *IEEE Trans. Ind. Electron.*, vol. 55, no. 12, pp. 4312–4324, Dec. 2008.

[5] T. Geyer, P. Karamanakos, and R. Kennel, "On the benefit of long-horizon direct model predictive control for drives with $LC$ filters," in *Proc. IEEE Energy Convers. Congr. Expo.*, Pittsburgh, PA, USA, Sep. 2014, pp. 3520–3527.

[6] T. Geyer and D. E. Quevedo, "Multistep finite control set model predictive control for power electronics," *IEEE Trans. Power Electron.*, vol. 29, no. 12, pp. 6836–6846, Dec. 2014.

[7] P. Karamanakos, T. Geyer, N. Oikonomou, F. D. Kieferndorf, and S. Manias, "Direct model predictive control: A review of strategies that achieve long prediction intervals for power electronics," *IEEE Ind. Electron. Mag.*, vol. 8, no. 1, pp. 32–43, Mar. 2014.

[8] P. Acuña, C. Rojas, R. Baidya, R. P. Aguilera, and J. Fletcher, "On the impact of transients on multistep model predictive control for medium-voltage drives," *IEEE Trans. Power Electron.*, vol. 34, no. 9, pp. 8342–8355, Sep. 2019.

[9] T. Dorfling, H. du Toit Mouton, T. Geyer, and P. Karamanakos, "Long-horizon finite-control-set model predictive control with nonrecursive sphere decoding on an FPGA," *IEEE Trans. Power Electron.*, vol. 35, no. 7, pp. 7520–7531, Jul. 2020.

[10] E. Liegmann, P. Karamanakos, and R. Kennel, "Real-time implementation of long-horizon direct model predictive control on an embedded system," *IEEE Open J. Ind. Appl.*, vol. 3, pp. 1–12, 2022.

[11] P. Karamanakos, E. Liegmann, T. Geyer, and R. Kennel, "Model predictive control of power electronic systems: Methods, results, and challenges," *IEEE Open J. Ind. Appl.*, vol. 1, pp. 95–114, 2020.

[12] S. Baltruweit, E. Liegmann, P. Karamanakos, and R. Kennel, "FPGA-implementation friendly long-horizon finite control set model predictive control for high-power electronic systems," in *Proc. IEEE Energy Convers. Congr. Expo. Asia*, Singapore, Singapore, May 2021, pp. 1823–1828.

[13] G. Betti, M. Farina, and R. Scattolini, "A robust MPC algorithm for offset-free tracking of constant reference signals," *IEEE Trans. Autom. Control*, vol. 58, no. 9, pp. 2394–2400, Sep. 2013.

[14] L. Yan, F. Wang, M. Dou, Z. Zhang, R. Kennel, and J. Rodríguez, "Active disturbance-rejection-based speed control in model predictive control for induction machines," *IEEE Trans. Ind. Electron.*, vol. 67, no. 4, pp. 2574–2584, Apr. 2020.

[15] L. Yan and X. Song, "Design and implementation of Luenberger model-based predictive torque control of induction machine for robustness improvement," *IEEE Trans. Power Electron.*, vol. 35, no. 3, pp. 2257–2262, Mar. 2020.

[16] O. Wallscheid and E. F. B. Ngoumtsa, "Investigation of disturbance observers for model predictive current control in electric drives," *IEEE Trans. Power Electron.*, vol. 35, no. 12, pp. 13563–13572, Dec. 2020.

[17] J. L. Zamora and A. Garcia-Cerrada, "Online estimation of the stator parameters in an induction motor using only voltage and current measurements," *IEEE Trans. Ind. Appl.*, vol. 36, no. 3, pp. 805–816, May/Jun. 2000.

[18] M. Yang, X. Lang, J. Long, and D. Xu, "Flux immunity robust predictive current control with incremental model and extended state observer for PMSM drive," *IEEE Trans. Power Electron.*, vol. 32, no. 12, pp. 9267–9279, Dec. 2017.

[19] X. Zhang, L. Zhang, and Y. Zhang, "Model predictive current control for PMSM drives with parameter robustness improvement," *IEEE Trans. Power Electron.*, vol. 34, no. 2, pp. 1645–1657, Feb. 2019.

[20] O. Lipcak and J. Bauer, "MRAS-based induction machine magnetizing inductance estimator with included effect of iron losses and load," *IEEE Access*, vol. 9, pp. 166234–166248, 2021.

[21] C.-K. Lin, J.-t. Yu, Y.-S. Lai, and H.-C. Yu, "Improved model-free predictive current control for synchronous reluctance motor drives," *IEEE Trans. Ind. Electron.*, vol. 63, no. 6, pp. 3942–3953, Jun. 2016.

[22] F. Tinazzi, P. G. Carlet, S. Bolognani, and M. Zigliotto, "Motor parameter-free predictive current control of synchronous motors by recursive least square self-commissioning model," *IEEE Trans. Ind. Electron.*, vol. 67, no. 11, pp. 9093–9100, Nov. 2020.

[23] M. Khalilzadeh, S. Vaez-Zadeh, J. Rodriguez, and R. Heydari, "Model-free predictive control of motor drives and power converters: A review," *IEEE Access*, vol. 9, pp. 105733–105747, 2021.

[24] T. Geyer, *Model predictive control of high power converters and industrial drives*. Hoboken, NJ, USA: Wiley, 2016.

[25] A. M. Alturas, S. M. Gadoue, B. Zahawi, and M. A. Elgendy, "On the identifiability of steady-state induction machine models using external measurements," *IEEE Trans. Energy Convers.*, vol. 31, no. 1, pp. 251–259, Mar. 2016.

[26] G. Slemon, "Modelling of induction machines for electric drives," *IEEE Trans. Ind. Appl.*, vol. 25, no. 6, pp. 1126–1131, Nov./Dec. 1989.

[27] R. P. Aguilera and D. E. Quevedo, "Predictive control of power converters: Designs with guaranteed performance," *IEEE Trans. Ind. Inf*, vol. 11, no. 1, pp. 53–63, Feb. 2015.

[28] P. Karamanakos, T. Geyer, and R. Kennel, "On the choice of norm in finite control set model predictive control," *IEEE Trans. Power Electron.*, vol. 33, no. 8, pp. 7105–7117, Aug. 2018.

[29] R. P. Aguilera and D. E. Quevedo, "Stability analysis of quadratic MPC with a discrete input alphabet," *IEEE Trans. Autom. Control*, vol. 58, no. 12, pp. 3190–3196, Dec. 2013.

[30] P. Karamanakos, T. Geyer, and R. Kennel, "A computationally efficient model predictive control strategy for linear systems with integer inputs," *IEEE Trans. Control Syst. Technol.*, vol. 24, no. 4, pp. 1463–1471, Jul. 2016.

[31] L. Ortombina, P. Karamanakos, and M. Zigliotto, "Robustness analysis of long-horizon direct model predictive control: Induction motor drives," in *Proc. IEEE Workshop on Control and Model. for Power Electron.*, Aalborg, Denmark, Nov. 2020, pp. 1–8.

[32] B. Arif, L. Tarisciotti, P. Zanchetta, J. C. Clare, and M. Degano, "Grid parameter estimation using model predictive direct power control," *IEEE Trans. Ind. Appl.*, vol. 51, no. 6, pp. 4614–4622, Nov./Dec. 2015.

[33] M. A. W. Begh, P. Karamanakos, T. Geyer, and Q. Yang, "Gradient-based predictive pulse pattern control of medium-voltage drives—Part II: Performance assessment," *IEEE Trans. Power Electron.*, vol. 37, no. 12, pp. 14237–14251, Dec. 2022.

**Andrei Tregubov** (S'21) received the B.Sc. degree in electrical power engineering and M.Sc. degree in automation of energy systems from Peter the Great St. Petersburg Polytechnic University, Russia, in 2013 and 2015, respectively. In 2015 he received the M.Sc. diploma in electrical engineering/industrial electronics from Lappeenranta University of Technology, Finland, under the double degree program.

Since 2020 he has been working towards the Ph.D. degree in electrical engineering with the Faculty of Information Technology and Communication Sciences, Tampere University, Finland. His research interests include model predictive control of electrical drive systems, parameter estimation techniques, and the embedded implementation of control algorithms.

**Petros Karamanakos** (S'10–M'14–SM'19) received the Diploma and Ph.D. degrees in electrical and computer engineering from the National Technical University of Athens (NTUA), Athens, Greece, in 2007, and 2013, respectively.

From 2010 to 2011 he was with the ABB Corporate Research Center, Baden-Dättwil, Switzerland, where he worked on model predictive control strategies for medium-voltage drives. From 2013 to 2016 he was a PostDoc Research Associate in the Chair of Electrical Drive Systems and Power Electronics, Technische Universität München, Munich, Germany. Since 2016, he has been with the Faculty of Information Technology and Communication Sciences, Tampere University, Tampere, Finland, where he is currently an Associate Professor. His main research interests lie at the intersection of optimal control, mathematical programming and power electronics, including model predictive control and optimal modulation for power electronic converters and ac variable speed drives.

Dr. Karamanakos received the 2014 Third Best Paper Award of the IEEE Transactions on Industry Applications and two Prize Paper Awards at conferences. He serves as an Associate Editor of the IEEE Transactions on Industry Applications and of the IEEE Open Journal of Industry Applications. He is a Regional Distinguished Lecturer of the IEEE Power Electronics Society in the years 2022 and 2023.

**Ludovico Ortombina** (M'19) received the M.Sc. and Ph.D. degrees in mechatronics engineering from the University of Padova, Italy, in 2015 and 2019, respectively. Since August 2020, he has been a Researcher with the Department of Industrial Engineering, University of Padova. His research interests include parameter estimation techniques for synchronous motors, sensorless controls, and predictive control.